DOI: 10.13009/EUCASS2019-224



# Simulating vibrated fluids and vibroequilibria in the CFVib microgravity experiment

*Salgado Sánchez, P.*[*†]*, Fernández, J.*[⋆]*, Tinao, I.*[*]*, Porter, J.*[*] *and Bello, A.*[*]
[*]*E-USOC, Ciencias y Operaciones Aeroespaciales, Center for Computational Simulation, DAVE, ETSIAE, Universidad Politécnica de Madrid, Plaza Cardenal Cisneros 3, 28040 Madrid, Spain*
[⋆]*E-USOC, Ciencias y Operaciones Aeroespaciales, Center for Computational Simulation, DMAIA, ETSIAE, Universidad Politécnica de Madrid, Plaza Cardenal Cisneros 3, 28040 Madrid, Spain*
pablo.salgado@upm.es · jose.ffraile@upm.es · ignacio.tinao@upm.es · jeff.porter@upm.es · alvaro.bello@upm.es
[†]Corresponding author

## Abstract

The CFVib experiment investigated the use of piezoelectric actuators to manipulate fluids via the vibroequilibria effect. A model is developed to simulate fluid behaviour in this experiment, including interaction with the container and piezoelectrics. Since vibroequilibria evolve slowly compared to the applied forcing, a separation of timescales is used to obtain a linear problem on the fast timescale whose solution provides a quasisteady source term driving slow vibroequilibria dynamics. We find that the surface adopts different vibroequilibria depending on the selected mode of vibration. Simulations show good agreement with experiments and suggest a potential strategy for manipulating fluids in weightlessness.

## 1. Introduction

By their nature, fluids move easily and adjust their shape and position in response to external forces. In the presence of a gravitational field, a large body of liquid will minimize its height by pooling in the lowest configuration possible, with the interface generally flat and horizontal. External forcing can change this situation, driving the fluid to a new equilibrium and/or supporting excitations on the surface or in the bulk. Periodic forcing, for example, is relatively common and easy to apply, affects important phenomena like mixing and mass transfer, and has broad significance in engineering and biological systems. Periodic vibrations have the potential to destabilize the flat surface equilibrium, as with the well-known phenomenon of Faraday waves,[1] or to stabilize an otherwise unstable configuration, as with the Rayleigh-Taylor instability.[2]

The effects of vibrations on such systems can be roughly divided according to the forcing frequency and orientation. Low-frequency vibrations (provided they are not purely perpendicular to the surface) tend to excite back-and-forth motion along the axis of vibration, or sloshing modes.[3] Higher frequencies can excite interfacial waves, which may be harmonic, with the same period as the forcing, or subharmonic,[4] with twice that period. The associated patterns, whose wavelength is often smaller than the system length scale, can display complex dynamics and transition scenarios, a subject of much interest in recent decades.[5]

The orientation is another key factor in determining the fluid response. If the forcing is applied perpendicular to a large flat surface, the flat solution persists and undergoes a parametric instability[6] to (typically) subharmonic surface waves beyond a certain forcing threshold.[7] These waves extend over the entire surface since, aside from boundary effects, the forcing can be considered homogeneous throughout the domain. Horizontal (more generally, non-vertical) forcing directly produces harmonic waves and, in many situations, subharmonic waves such as cross-waves.[8,9] In contrast to the case of vertical motion, these wave fields are concentrated near the rigid boundaries, which act as wavemakers. In a horizontally vibrated rectangular container the interaction between wave fields extending from opposite endwalls can induce temporal modulations[10] and a variety of secondary bifurcations,[11] depending on the extent to which they penetrate into the interior of the container.

In addition to surface waves and other phenomena that evolve on the fast timescale of the forcing, the fluid may respond to average effects on a slower timescale, as with the Kelvin-Helmholtz instability in density-stratified systems. Vibrations parallel to density contours can excite, at a critical forcing amplitude, quasisteady waves known as frozen waves.[12–14] If the frozen wave instability is observed in a two-fluid system in weightlessness, the typical sinusoidal pattern at onset develops rapidly into a larger columnar structure, eventually forming a series of vertical

DOI: 10.13009/EUCASS2019-224



interfaces separating alternating volumes of the different liquids.[15,16] Recent experiments[17,18] have shown that, after this frozen wave column growth, Faraday waves can then be excited along the nearly vertical interfaces, thus producing an interesting two-scale wave pattern. In this complex scenario, the pattern selection problem is not only controlled by the vibrational velocity, but is strongly affected by viscosity[13] and finite-size effects.[19,20]

Another slow timescale phenomenon driven by periodic vibrations concerns the reorientation of the fluid toward a new quasisteady equilibrium, which may differ considerably from the hydrostatic one. This behaviour, first observed in 1831 by Faraday[1] in the flattening of fluid drops suspended beneath a vibrating plate, is known as the vibroequilibria effect. Like frozen waves, vibroequilibria are supported by the oscillatory velocity field generated by the applied vibrations. It is the spatial inhomogeneity of this field, and the corresponding oscillatory pressure gradient, that leads to deformation of the surface. Recent analysis,[21] using both numerical and theoretical techniques, found that, for deep enough layers of fluid, symmetric vibroequilibria in horizontally vibrated rectangular containers can suffer a disordered transition to one of many possible asymmetric solutions. In low-viscosity fluids, surface wave dynamics may also lead to the destruction of vibroequilibria states due to nonlinear forcing of the first (odd) sloshing mode and its potentially unbounded growth.

In reduced gravity environments, fluids behave differently than on ground. Surface tension is no longer dominated by gravity, so there is no preference for flat surfaces. A floating volume of liquid will minimize its surface energy by taking a spherical shape, while capillary forces may cause a confined liquid to fully wet the boundaries. The curved surfaces promoted by the forces of cohesion and adhesion mean that the distinction between vertical and horizontal forcing is of limited value. Any applied external force will be inhomogeneous over such a surface. Nonetheless, it can be useful to identify effective local forcing orientations over particular portions of the surface and thus, to understand the behaviour and surface dynamics as a combination of the more familiar phenomena observed on Earth and their interaction.[18] The absence of a strong gravitational force has a marked effect on vibroequilibria as well, which deviate much more from the unforced equilibrium since, in weightlessness, the vibrational energy that drives this movement only needs to balance surface and contact energies and becomes comparable for small to moderate forcing amplitudes.

The facility that fluids have to adjust their shape when forced, combined with the preference for curved hydrostatic surfaces, means that fluid management in microgravity is different and often more complicated than it is on Earth. Although vibrations are frequently unwanted in a space environment, they may also, potentially, be put to good use. For example, vibrations are under consideration to help reducing muscle and bone loss in astronauts, and can mimic the effects of gravity in other ways too.[22] This includes the potential to induce convection, which has critical implications in physical processes like mixing, heat transfer, and phase separation.

Further understanding of the various effects of vibrations on fluids may make it possible to use them for advantage in space systems to deliberately manipulate and control fluids, which is a critical problem in space travel. The vibroequilibria effect, in particular, suggests artificial gravity since, as the forcing amplitude increases, the interface tends to evolve toward a more perpendicular alignment with respect to the axis of vibration, restoring some degree of the familiar preference for flat interfaces. The Control of Fluids in microgravity with Vibrations (CFVib) experiment[23] examined the dynamic behaviour of representative fluids combinations subjected to vibrations. The data obtained contribute to understanding the vibroequilibria effect, and help demonstrate the potential of vibrations for manipulating fluids in microgravity.

In this paper, we present the numerical model used to simulate the vibroequilibria effect in the CFVib experiment. In Sec. 2, the experimental setup is briefly described. In Sec. 3, the mathematical formulation of the vibrated fluid problem, based on separation of timescales, is described. This formulation includes a model of the interaction between the fluid, structure, and piezoelectric actuators. In Sec. 4, the algorithm and numerical scheme is presented. General predictions of the model are presented in Sec. 5 and compared to experiments on ground and in microgravity in Sec. 6. Conclusions are given in Sec. 7.

## 2. The CFVib experiment

The main objective of the experiment is to observe the vibroequilibria effect in small fluid volumes in microgravity. Under reduced gravity conditions, vibroequilibria theory predicts the general tendency of fluid interfaces to orientate more perpendicular to the axis of applied vibrations.[21,24]

The heart of the experiment is a small recipient (several centimetres wide) that is subjected to high frequency vibrations and either half-filled with water or silicone oil, or filled completely with a combination of silicone oil and vacuum oil. We focus here on the first two liquid-air configurations, which yielded better results than the two-liquid experiment. The recipient, which is cuboidal or cylindrical, is attached to an aluminium beam in a cantilever configuration with two piezoelectric ceramics attached on opposite horizontal faces near the clamped end. Fig. 1 shows (a) a cuboidal container holding the oil-oil combination and (b) a cylindrical container holding water.

DOI: 10.13009/EUCASS2019-224



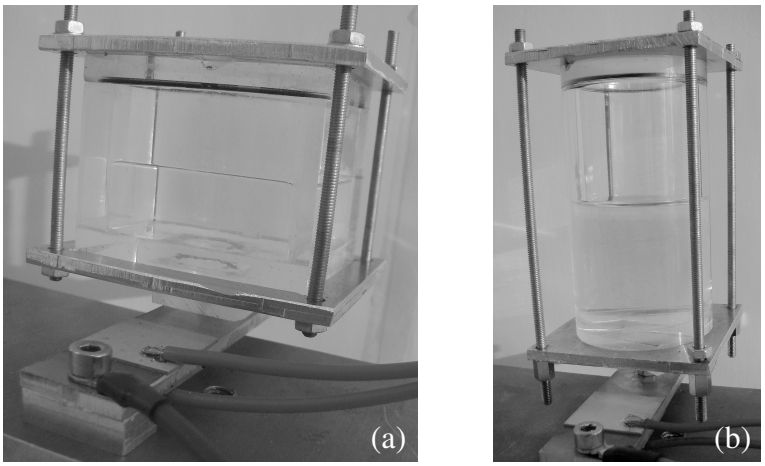


Figure 1: Images of the experimental cells: (a) cuboid and (b) cylinder. The piezoelectric ceramic attached on the upper side of the beam (the other is attached underneath) is visible in each assembly along with the associated cabling.

The pair of piezoelectric ceramics are electrically excited in counterphase to induce a linear distribution of tensile stress along the beam width. This stress generates a bending moment that drives flexural vibrations without longitudinal motion. The electrical signals driving the vibrations are passed through an acoustic amplifier to boost the power transmitted. The two main control parameters are voltage amplitude and frequency, which select the character of the applied vibrations. The amplitude of vibrations can be varied in a (nearly) continuous manner. The driving frequency, on the other hand, is selected to coincide with one of the many structural resonances, where larger displacements can be achieved. The resonances explored include both flexural beam modes and container modes, located at particular values over the range of 50 Hz to 12 kHz. Dedicated cabling is attached to each piezoelectric to transmit the electrical signals, and part of this can be seen in Fig. 1. The fluid dynamics is monitored by means of a charge-coupled device (CCD) camera using an acquisition rate of (approximately) 20 frames per seconds, which is enough to capture the average effects of the applied vibrations.

The microgravity experiments are thus defined by the selected fluid(s), container geometry and applied voltage (peak-to-peak amplitude and frequency). They were conducted on board an aircraft executing parabolic flight manoeuvres to provide repeated periods of approximately 20 s of reduced gravity. Since the different fluids have different surface tension and contact angles, a comparison reveals something of their influence on the vibrational phenomena. To observe clear vibroequilibria effects, the energy associated with the oscillatory velocity field should be (at least locally) greater or comparable to the characteristic variation in contact and surface energies. For experiments with silicone oil, which has a low contact angle (with most solids) and wets easily, this can be expected to be somewhat easier to achieve because contact angle, and thus contact energy, will be nearly constant. The experiments with water, in contrast, have more resistance to contact line motion.

In order to separate the effects of the forcing from accelerations caused by the aircraft (residual gravity or g-jitter), an unforced cell was included for each configuration. These passive cells have no piezoelectrics to excite the bender beam but are otherwise identical (to the extent possible). Further details of the experiment setup can be found in Fernández et al. (2017).[23]

## 3. Mathematical formulation

The experiments described in Sec. 2 depend on the complex interaction of different physical systems. The mathematical formulation presented below includes a treatment of fluid dynamics under a vibrational field (detailed in Sec. 3.1), the electromechanical coupling of piezoelectric materials and the structural assemblies that governs the conversion of electrical power into mechanical motion (detailed in Sec. 3.2), and the fluid-structure interaction, which determines how structural displacements generate fluid motion. Altogether, the mathematical model describes the transfer of electrical energy into the fluid and, in particular, to surface deformation.

DOI: 10.13009/EUCASS2019-224



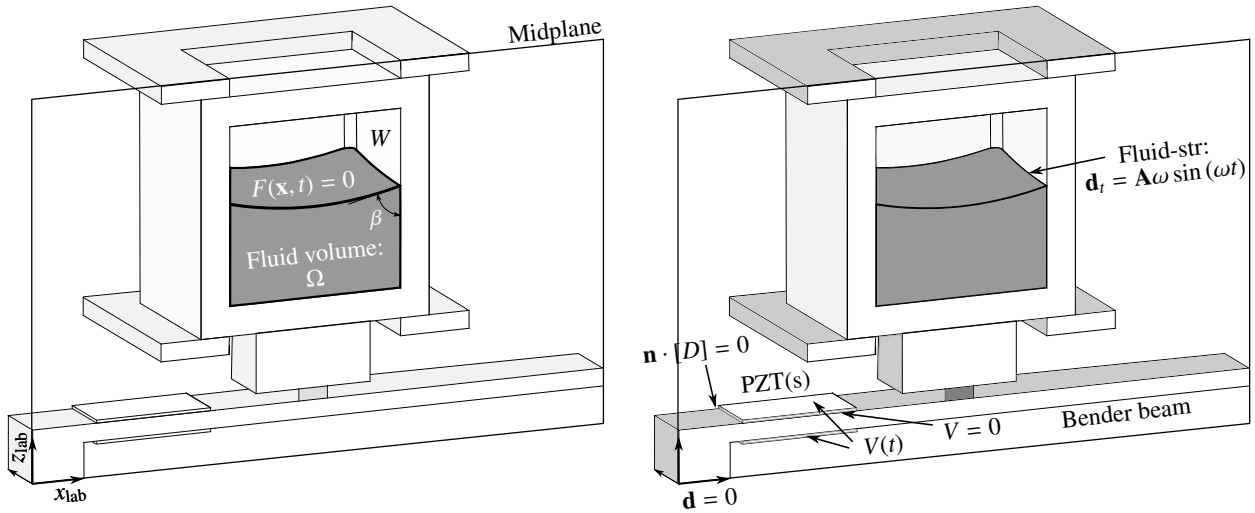


(a) Fluid dynamics

(b) Fluid–structure–piezoelectric interaction

Figure 2: Sketches showing a midplane cut of the cuboid assembly. The domains of the mathematical formulation for (a) fluid dynamics and (b) fluid-structure-piezoelectric interaction are included. Throughout this paper, simulations assume the midplane reflection symmetry illustrated here.

### 3.1 Fluid dynamics

We consider a volume $\Omega$ of fluid held in a vibrated container in the presence of a gravitational field [see Fig. 2(a)]. The fluid satisfies the incompressible Navier-Stokes momentum and mass continuity equations[25]

$$\rho\,[\mathbf{u}_t + (\mathbf{u}\cdot\nabla)\,\mathbf{u}] = -\nabla p + \mu\,\Delta\mathbf{u} + \rho\,\mathbf{g}\,(t), \tag{1a}$$

$$\nabla\cdot\mathbf{u} = 0, \tag{1b}$$

where $\mathbf{u}$ is the velocity, $\rho$ the density, $\mu$ the dynamic viscosity, $p$ the pressure, and $\mathbf{g}\,(t)$ the gravitational acceleration.

No-slip boundary conditions apply on the solid boundaries $W\,(\mathbf{x}, t)$, which oscillate with frequency $\omega$ in the laboratory reference frame. On the free surface $F(\mathbf{x}, t) = 0$, there is a balance between surface tension, pressure and viscous stress.

$$\mathbf{u} = \mathbf{A}\omega\,\sin\,(\omega t), \qquad \text{on } W\,(\mathbf{x}, t); \tag{2a}$$

$$p\,\mathbf{n} - (\Gamma\kappa)\,\mathbf{n} - \mu\,(\nabla\mathbf{u})\cdot\mathbf{n} = 0, \qquad \text{on } F\,(\mathbf{x}, t); \tag{2b}$$

$$F_t + \mathbf{u}\cdot\nabla F = 0, \qquad \text{on } F\,(\mathbf{x}, t). \tag{2c}$$

Here, $\kappa$ is the mean curvature of the interface defined as

$$2\,\kappa(F) = \nabla\cdot\left(\frac{\nabla F}{|\nabla F|}\right), \tag{3}$$

where $\mathbf{n} = \nabla F/|\nabla F|$ is a unit normal vector and $\mathbf{A}(\mathbf{x})$ describes the spatial distribution of the boundary displacement.

For the experiments of Sec. 2, the applied vibrations are of small amplitude, $|\mathbf{A}| \ll L$, and high frequency $\omega \gg \mu/(\rho\,L^2)$, where $L$ is the characteristic length of the container. This allows a separation of timescales[12] to be applied, with different descriptions for phenomena occurring on the slow (vibroequilibria) timescale $t_v = t$ and the fast (harmonic) timescale $t_h = \omega t$. Fluid velocity and pressure are expressed as the sum of contributions from each of these timescales,

$$\mathbf{u} = \mathbf{u}_h\,(\boldsymbol{x}, t_h) + \omega^{-1}\mathbf{u}_v\,(\boldsymbol{x}, t_v) + \ldots\,, \tag{4a}$$

$$p = \omega\,p_h\,(\boldsymbol{x}, t_h) + \;p_v\,(\boldsymbol{x}, t_v) + \ldots\,, \tag{4b}$$

$$F = F\,(\boldsymbol{x}, t) + \ldots\,, \tag{4c}$$

while temporal derivatives are written as

$$(\cdot)_t = \omega\,(\cdot)_{t_h} + (\cdot)_{t_v}\,. \tag{5}$$

DOI: 10.13009/EUCASS2019-224



The (imperfect) gravity level of the parabolic flight typically satisfies $|\mathbf{g}| < 0.05\,\mathrm{g}_0$,[26] where $\mathrm{g}_0 = 9.81$ m/s$^2$. In situ measurements demonstrate that the dominant microgravity variations occur on the slow timescale, so that we may write $\mathbf{g} = \mathbf{g}(t_v)$. The appropriate fluid equations in this limit are derived below, where it's also assumed, for simplicity, that $\mathbf{g} = 0$ (i.e., no residual gravity). Relaxing this final condition does not change the mathematical formulation.

#### 3.1.1 Fast timescale dynamics: Linear harmonic field

The dynamics on the fast (harmonic) timescale, which occur in response to the motion of the walls $W$, satisfy

$$\rho\,\mathbf{u}_{h,\,t_h} = -\nabla p_h + \mu\,\Delta\mathbf{u}_h \qquad \text{in } \Omega, \tag{6a}$$
$$\nabla\cdot\mathbf{u}_h = 0 \qquad \text{in } \Omega, \tag{6b}$$
$$\mathbf{u}_h = \mathbf{A}\omega\,\sin(\omega t) \qquad \text{on } W, \tag{6c}$$
$$p_h = 0 \qquad \text{on } F, \tag{6d}$$
$$F_{t_h} = 0 \qquad \text{on } F, \tag{6e}$$

where the viscous term is retained in the momentum equation to preserve no-slip boundary conditions on the solid boundaries. The free surface does not evolve on the fast timescale [Eq. (6e)] and the force balance reduces to a constant (zero) pressure condition [Eq. (6d)].

#### 3.1.2 Slow timescale dynamics: Mean flow field

The dynamics of the mean flow occurring on the slow timescale are driven by gravity (neglected here) and the convective term arising from the fast (harmonic) velocity field. As per the separation of timescales, this latter source term is averaged over one period,[12] denoted by $\langle\cdot\rangle$, to obtain the governing equations

$$\rho\left[\mathbf{u}_{v,\,t_v} + \langle(\mathbf{u}_h\cdot\nabla)\,\mathbf{u}_h\rangle\right] = -\nabla p_v + \mu\,\Delta\mathbf{u}_v \qquad \text{in } \Omega, \tag{7a}$$
$$\nabla\cdot\mathbf{u}_v = 0 \qquad \text{in } \Omega, \tag{7b}$$
$$\mathbf{u}_v = 0 \qquad \text{on } W, \tag{7c}$$
$$p_v\,\mathbf{n} - (\Gamma\kappa)\,\mathbf{n} - \mu\,(\nabla\mathbf{u}_v)\cdot\mathbf{n} = 0 \qquad \text{on } F, \tag{7d}$$
$$F_{t_v} + \mathbf{u}_v\cdot\nabla F = 0 \qquad \text{on } F. \tag{7e}$$

Again, viscous terms are retained in order to have no-slip boundary conditions on the solid walls.

Note that Eqs. (6) are coupled to Eqs. (7) through the evolution of the free surface $F$, which defines the fluid domain $\Omega$. It is thus necessary to solve both the fast and slow timescale equations in an iterative manner. Further simplifications of this approach can be made in some cases, as described in subsequent sections.

### 3.2 Piezoelectricity and Structural mechanics

The general formulation of piezoelectricity is in terms of differential equations describing the balance of momentum and energy conservation[27]

$$\rho_m\,\mathbf{d}_{tt} - \nabla\cdot[S] = \mathbf{p}, \tag{8a}$$
$$\nabla\cdot\mathbf{D} = \rho_v, \tag{8b}$$

where $\rho_m$ is the density of the material in question, $\rho_v$ is the charge density, $\mathbf{d}$ is a vector of displacements, $[S]$ is the (symmetric) mechanical stress tensor, $\mathbf{p}$ contains the volume forces acting on the piezoelectric material (or structure) and $\mathbf{D}$ is the electrical displacement. This electrical displacement is produced by charge distribution gradients in the element due to deformation in the molecular structure.[28]

Equations (8) are closed with the classical constitutive law

$$[\epsilon] = \frac{1}{2}\left(\nabla\mathbf{d} + (\nabla\mathbf{d})^T\right), \tag{9}$$

where $[\epsilon]$ is the (symmetric) mechanical strain tensor, the Maxwell equation relating the electric field $\mathbf{E}$ and voltage $V$

$$\mathbf{E} = -\nabla V, \tag{10}$$

DOI: 10.13009/EUCASS2019-224



and the material constitutive relationships

$$\begin{pmatrix} \epsilon_{11} \\ \epsilon_{12} \\ \epsilon_{13} \\ \epsilon_{22} \\ \epsilon_{23} \\ \epsilon_{33} \\ D_1 \\ D_2 \\ D_3 \end{pmatrix} = \begin{pmatrix} s^E_{11} & s^E_{12} & s^E_{13} & s^E_{14} & s^E_{15} & s^E_{16} & d^M_{11} & d^M_{12} & d^M_{13} \\ s^E_{21} & s^E_{22} & s^E_{23} & s^E_{24} & s^E_{25} & s^E_{26} & d^M_{21} & d^M_{22} & d^M_{23} \\ s^E_{31} & s^E_{32} & s^E_{33} & s^E_{34} & s^E_{35} & s^E_{36} & d^M_{31} & d^M_{32} & d^M_{33} \\ s^E_{41} & s^E_{42} & s^E_{43} & s^E_{44} & s^E_{45} & s^E_{46} & d^M_{41} & d^M_{42} & d^M_{43} \\ s^E_{51} & s^E_{52} & s^E_{53} & s^E_{54} & s^E_{55} & s^E_{56} & d^M_{51} & d^M_{52} & d^M_{53} \\ s^E_{61} & s^E_{62} & s^E_{63} & s^E_{64} & s^E_{65} & s^E_{66} & d^M_{61} & d^M_{62} & d^M_{63} \\ d^E_{11} & d^E_{12} & d^E_{13} & d^E_{14} & d^E_{15} & d^E_{16} & \epsilon^M_{11} & \epsilon^M_{12} & \epsilon^M_{13} \\ d^E_{21} & d^E_{22} & d^E_{23} & d^E_{24} & d^E_{25} & d^E_{26} & \epsilon^M_{21} & \epsilon^M_{22} & \epsilon^M_{23} \\ d^E_{31} & d^E_{32} & d^E_{33} & d^E_{34} & d^E_{35} & d^E_{36} & \epsilon^M_{31} & \epsilon^M_{32} & \epsilon^M_{33} \end{pmatrix} \begin{pmatrix} S_{11} \\ S_{12} \\ S_{13} \\ S_{22} \\ S_{23} \\ S_{33} \\ E_1 \\ E_2 \\ E_3 \end{pmatrix}. \tag{11}$$

Here, $s^E_{ij}$ are the elastic coefficients, $d^M_{ij}$ and $d^E_{ij}$ are the piezoelectric coefficients and $\epsilon^M_{ij}$ is the dielectric permittivity.[29] For classical structural elements that do not couple to the electric field, this same formulation holds but with $d^M_{ij} = d^E_{ij} = \epsilon^M_{ij} = 0$. The formulation may be extended to include damping, as described in later sections.

Different boundary conditions are applied for the piezoelectric material compared to ordinary materials:

(i) The electrical problem in the piezoelectric ceramics is solved by imposing ground voltage on the faces adjacent to the beam and the periodic voltage $V_0 = (V_{pp}/2)\sin(\omega t)$ of frequency $\omega$ on the opposite horizontal sides. Zero charge is enforced on the remaining boundaries.

(ii) For ordinary material elements, zero displacement and stress are imposed at the fixed and free boundaries, respectively. Interfaces separating structural elements are considered to fully transmit stresses and strains.

Since the structure vibrates harmonically at the frequency $\omega$ of the applied voltage, the fluid-structure interaction on $W$ is made consistent with the solution of Eqs. (8)–(11) by writing

$$\mathbf{d}_t = \mathbf{A}\,\omega\,\sin(\omega t). \tag{12}$$

Equations (6)–(12) are solved in dimensional variables with COMSOL Multiphysics 5.3[30] using the Finite Element Method. The numerical scheme is discussed below.

## 4. Numerical scheme

### 4.1 Algorithm

We solve the problem formulated in Sec. 3 with an iterative algorithm. Following the work of Koster (2006),[31] the dynamics on the fast timescale are solved first, including the fluid-structure interaction. The resulting linear field is then averaged to determine its contribution to the slow timescale, and the corresponding mean flow equations (7) are evolved through one or more forcing periods. After that, the free surface location is updated and the process is repeated. This algorithm is illustrated in Fig. 3(a) using solid lines (arrows).

We can distinguish several processes and characteristic timescales for the CFVib experiment:

(i) The timescale of the fast (harmonic) dynamics is $\omega^{-1} \sim 10^{-4} - 10^{-2}$ s, where frequencies up to tens of kHz are considered.[23]

(ii) The mean flow (vibroequilibria) timescale is on the order of seconds,[21] $t_v \sim 1 - 10$ s.

(iii) The timescale of sound waves propagating through the fluid is $L\,a^{-1} \sim 10^{-5}$ s, where $a = 1500$ m/s is the speed of sound in water and $L = 3$ cm is the characteristic length of the container.

(iv) The typical transient time to relax to an unforced hydrostatic equilibrium, as with vibroequilibria, is on the order of seconds.[32]

DOI: 10.13009/EUCASS2019-224



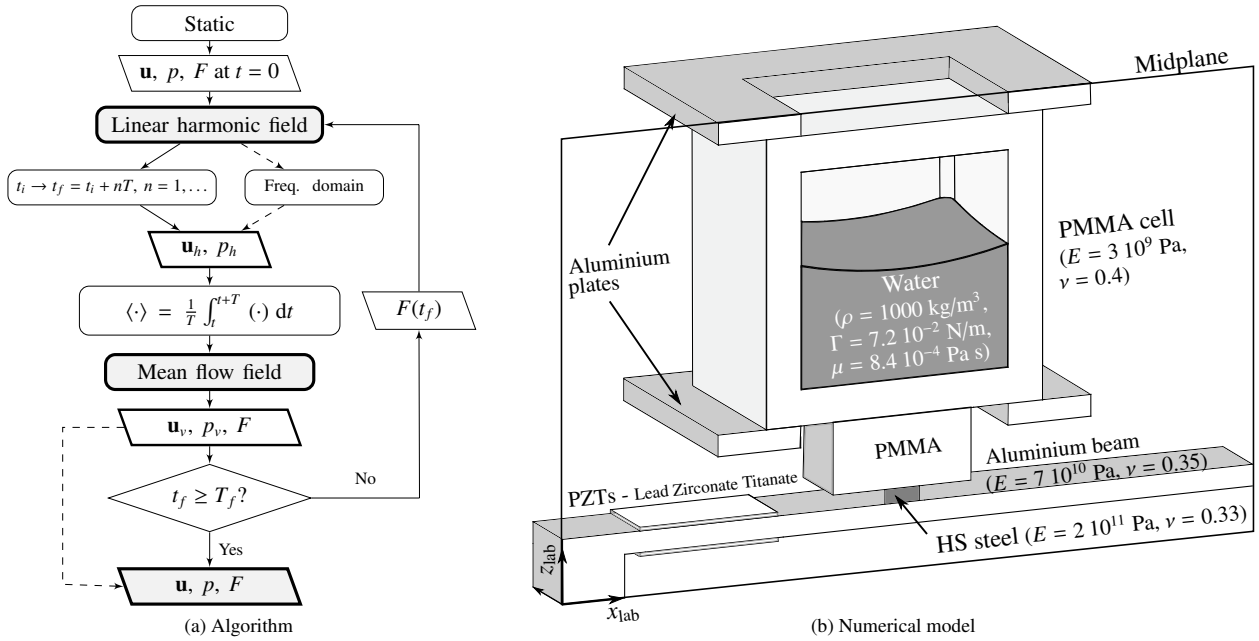


(a) Algorithm (b) Numerical model

Figure 3: (a) Algorithm using the timescales separation approach, showing the complete iterative scheme (solid lines) and the simplified scheme (dashed lines) followed here. Here $T$ is the forcing period and $T_f$ the stopping time. (b) The complete (symmetric) geometry used in the model. The relevant physical properties of water (at room temperature) and of structural materials, reproduced from the COMSOL Library, are included: density $\rho$, surface tension $\Gamma$, dynamic viscosity $\mu$, Young's modulus $E$ and Poisson ratio $\nu$, when applicable.

Since the mean flow evolves over a much longer timescale than the harmonic field and the propagation of its changes via sound waves, transient behaviour in the harmonic solution may be neglected, treating it as (quasi)steady. This allows the harmonic solution to be expressed in the frequency domain, which reduces the computational cost. Moreover, since the speed of wave propagation (i.e., sound) in solids is even larger than in fluids, this assumption can naturally be extended to the structural mechanics part of the problem. Transient behaviour is thus only considered as part of the mean flow problem, along with surface reorientation.

The solution of a linear problem gives the harmonic velocity field $\mathbf{u}_h$ in the fluid for a fixed geometry as discussed above. In the case of interest here, where the wavelength of sound (on the order of meters) is much larger than the characteristic length of the container (several centimetres), the fluid dynamics may be treated as incompressible. Furthermore, if the deformation of the surface (vibroequilibria) with respect to the static equilibrium is not large, then the same harmonic field can be used repeatedly for the source term in the mean flow equations without a large error, allowing a simplification of the basic algorithm and lower computing cost. In the simplest case, the effect of the surface deviation on the harmonic field is ignored completely and the same source term is used throughout the calculation.

The simplified numerical scheme, which does not update the harmonic fields $\mathbf{u}_h$ and $p_h$, is illustrated in Fig. 3(a) by dashed lines (arrows). Three steps are followed: (1) Solve the linear harmonic field in the frequency domain, and use the frequency dependence of the solution to locate resonances where more vigorous motion and a correspondingly enhanced vibroequilibria effect is expected, (2) calculate the (averaged) source term $\langle(\nabla\mathbf{u}_h)\,\mathbf{u}_h\rangle$ for the selected frequency, and (3) simulate the slow transient evolution toward the vibroequilibria solution at this frequency.

The linear harmonic field, resolved in the frequency domain, may be written as

$$\mathbf{u}_h = \frac{1}{2}\left(\mathbf{U}_h\,\mathrm{e}^{i\,\omega t} + \text{c.c.}\right), \tag{13}$$

where $\mathbf{U}_h(\mathbf{x})$ are complex functions, and "c.c." denotes the complex conjugate. The convective source term can then be written as

$$\langle(\nabla\mathbf{u}_h)\,\mathbf{u}_h\rangle = \frac{1}{4}\left(\nabla\mathbf{U}_h\bar{\mathbf{U}}_h + \nabla\bar{\mathbf{U}}_h\mathbf{U}_h\right), \tag{14}$$

where integrals of the form $\int_t^{t+2\pi/\omega}(\cdot)\,\mathrm{e}^{\pm 2i\omega t}\mathrm{d}t$ vanish, since $(\cdot)$ only depends on spatial coordinates. Note that this expression is assumed constant during the transient analysis, as discussed above, and is applied at the corresponding nodes in both the initial and deformed meshes.

DOI: 10.13009/EUCASS2019-224



| Mesh # | DoFs | $f_1$ (Hz) | $\lvert\Delta_1\rvert$ (%) | $f_2$ (Hz) | $\lvert\Delta_2\rvert$ (%) | $f_3$ (Hz) | $\lvert\Delta_3\rvert$ (%) | $\lvert\boldsymbol{\Delta}\rvert$ (%) |
|---|---|---|---|---|---|---|---|---|
| #1 | 19460 | 88 | 8.6 | 246 | 13.4 | 857 | 1.9 | 3.88 |
| #2 | 37168 | 86 | 6.2 | 240 | 10.6 | 846 | 0.5 | 2.76 |
| #3 | 56598 | 83 | 2.5 | 228 | 6.0 | 843 | 0.4 | 1.30 |
| **#4** | **118346** | **81** | **0.0** | **220** | **2.8** | **842** | **0.1** | **0.36** |
| Experiment | — | 81 | — | 217 | — | 841 | — | — |

Table 1: Results of the mesh convergence test against experimental measurements at the first three resonance frequencies. The selected mesh #4 is highlighted.

### 4.2 COMSOL model of the cuboid-water experiment

In the remainder of this paper, we apply the formulation of Sec. 3 to experiments in the cuboidal container that is half-filled with water. Figure 3(b) illustrates the geometry of the model, following the real container assembly as closely as possible. The vibrational dynamics of the system are principally affected by elements with relevant inertia or stiffness, so only these main elements are modelled. For example, neither the O-ring nor the screw-bolt unions (see Fig. 1), which are part of the real assembly, are retained in the model. Including these static compression loads does not modify the vibrational response in any significant way.

To model the experiment, we consider a rectangular cuboid with interior dimension (length × height × width) of 3 cm × 3 cm × 4 cm and solid walls of thickness of 0.5 cm. The cell is (approximately) half-filled with water. The dynamics of the contact line are simplified to impose a steady contact angle $\beta$ while permitting contact line motion; this is crucial to reproducing the experimental results. We remark that this numerical scheme does not consider the complications associated with contact line hysteresis, which may play a role in the experiments.

The container is made of PMMA (acrylic) and is closed by two aluminium plates to ensure one of the two levels of containment required in parabolic flights. We model the attachment to the bender beam using a PMMA piece and a steel nut, which act together as a support for the cell. The real mounting includes a bolt that is fastened to the PMMA block and later fastened to the beam. The PMMA block is chemically soldered to the container using chloroform. Finally, the beam geometry includes the two piezoelectric ceramics and the metal support piece on the clamped end, whose dimensions and location match the real experiment assembly.

The physical properties of water and the relevant material parts, which determine the constants and matrices involved in the governing Eqs. (6)-(12), are listed in Fig. 3(b). In particular, in the equations of piezoelectricity, many elements of $s_{ij}^E$, $d_{ij}^M$, $\epsilon_{ij}^M$ and $d_{ij}^E$ are either zero or determined by symmetries of the ceramic pieces. The experimental determination of these tensors has been undertaken by several investigations [see, e.g., Sherrit et al. (2007)[29]]. We do not attempt this precise characterization here, using instead the typical piezoelectric properties provided for Lead Zirconate Titanate (PZT-2) ceramic by the COMSOL Library.[30]

The unknown value of damping, which will be discussed more in subsequent sections, is taken to be small and equal for all structural elements: $\eta_s = 0.01,\ 0.02$ in the isotropic loss factor formulation (see Sec. 6.1 for details). We thus anticipate certain differences with the real experiments, especially regarding the predicted displacements in each mode. Further refinement of the model is done by determining the structural damping that best fits the experimental data at the resonance frequencies and including this frequency dependence.

For numerical convenience, a reflection symmetry about the midplane is assumed, which bars some types of dynamics (e.g., the first torsional mode of the beam is not permitted). We nonetheless expect to find good agreement with the experiments that are conducted near (non-torsional) resonances. For simulations of the free surface evolution, a BDF (backward differentiation formula) integration scheme is used with a *streamline* stabilization technique.

#### 4.2.1 Convergence of the numerical model

Convergence is examined for different meshes. The defining characteristics, results and numerical error compared to the experimental determination of the resonant modes, are included in Table 1. The simulations presented throughout this paper are performed using mesh #4, which gives acceptable accuracy with reasonable computing cost.

DOI: 10.13009/EUCASS2019-224



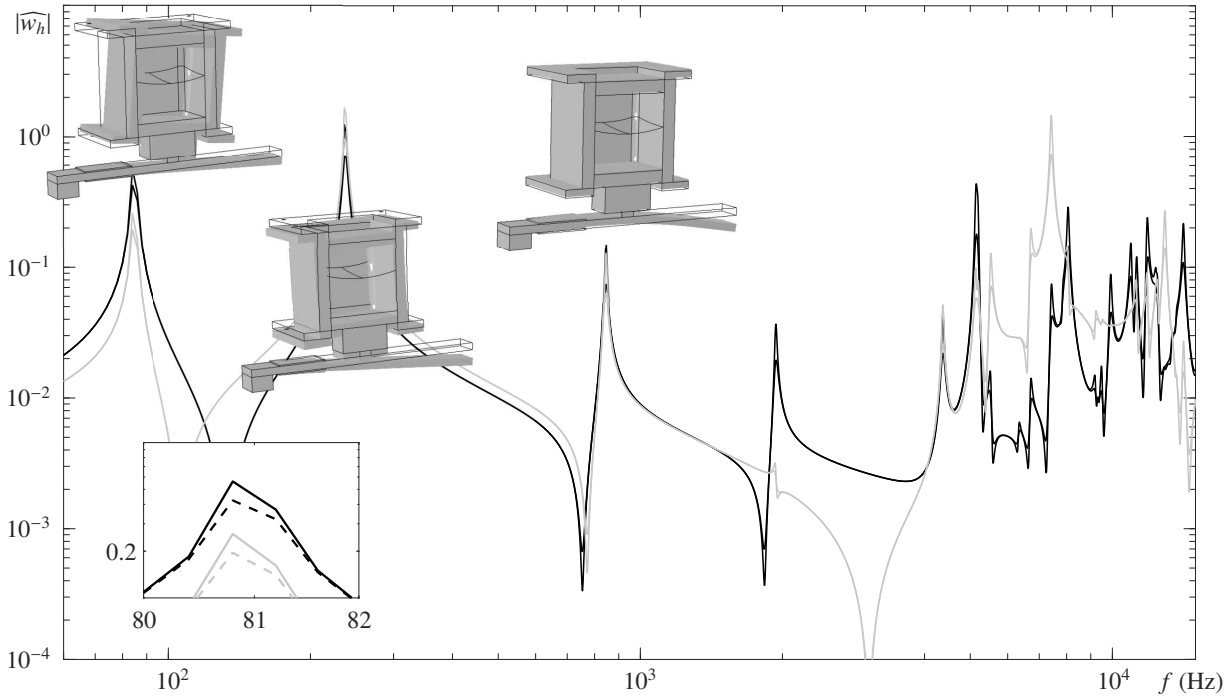


Figure 4: Magnitude of nondimensional harmonic velocity $|\widehat{w_h}|$ at the midpoint of the free surface (grey) and the midpoint of the right lateral wall (black) for different damping values $\eta_s = 0.01$ (solid) and 0.02 (dashed) with forcing $V_{pp} = 100\,\mathrm{V}$. A close-up view of the first resonance in the inset shows the effect of increased damping. The three first resonances near 81 Hz, 220 Hz and 842 Hz are illustrated at the instant of maximum deformation (displacement scale not preserved between illustrations).

## 5. Some numerical predictions

Following Fernandez at al. (2017),[21] we use the dimensionless velocity

$$(u_h,\, v_h,\, w_h) \to (\widehat{u_h},\, \widehat{v_h},\, \widehat{w_h})\left(\frac{\Gamma}{\rho\sqrt[3]{\mathcal{V}}}\right)^{0.5}, \tag{15}$$

where $\mathcal{V} = 18\,\mathrm{cm}^3$ is the volume of water used in the experiments. In Fig. 4, the absolute value of the dimensionless vertical velocity $|\widehat{w_h}|$ is calculated over the frequency range of interest for two selected damping values $\eta_s = 0.01$ (solid) and 0.02 (dashed lines) when the driving voltage has a peak-to-peak value $V_{pp} = 100\,\mathrm{V}$. Both the velocity at the midpoint of the fluid surface (grey) and at the right lateral PMMA wall (black line) where the accelerometer is placed in experiments, are shown. The importance of a resonance is evaluated in terms of the vertical velocity $\widehat{w_h}$ predicted at the free-surface; accordingly, any mode that does not induce substantial motion of the fluid is not considered.

Damping modifies the solution by limiting the maximum velocity (equivalently, displacement). As mentioned above, a wide variety of resonances, including a combination of flexural modes of the beam and modes of the cuboid structure, may be found. Special attention is paid to resonances at low frequency (less than 1 kHz) since these were found to be the most effective excitations in the experiment and can, also, be modelled more accurately because they are well-characterized by a single accelerometer measurement and require fewer mesh points.

The first resonance mode, near 81 Hz, involves the primary bending (rotational) motion of the cantilever beam that induces both vertical displacement and an in-phase rotation of the container, as sketched in the upper-left illustration of Fig. 4. This movement is complicated, but resembles a mixture of vertical (up-and-down motion at the midsection of the beam) and horizontal (due to rotation) excitations, which corresponds an oblique local vibrational axis. This interaction plays a key role in determining the vibroequilibria solution.

The second mode occurs near 220 Hz, and can be roughly understood as a combination of the primary bending (rotational) motion of the beam and a counterphase rotation of the container about the PMMA support. This mode provides an effective vibration (upper middle illustration) that induces vertical motion of roughly the same magnitude in the interior of the fluid as at the lateral wall.

Increasing the frequency to 842 Hz locates the third resonance, which involves the second flexural mode of the

DOI: 10.13009/EUCASS2019-224



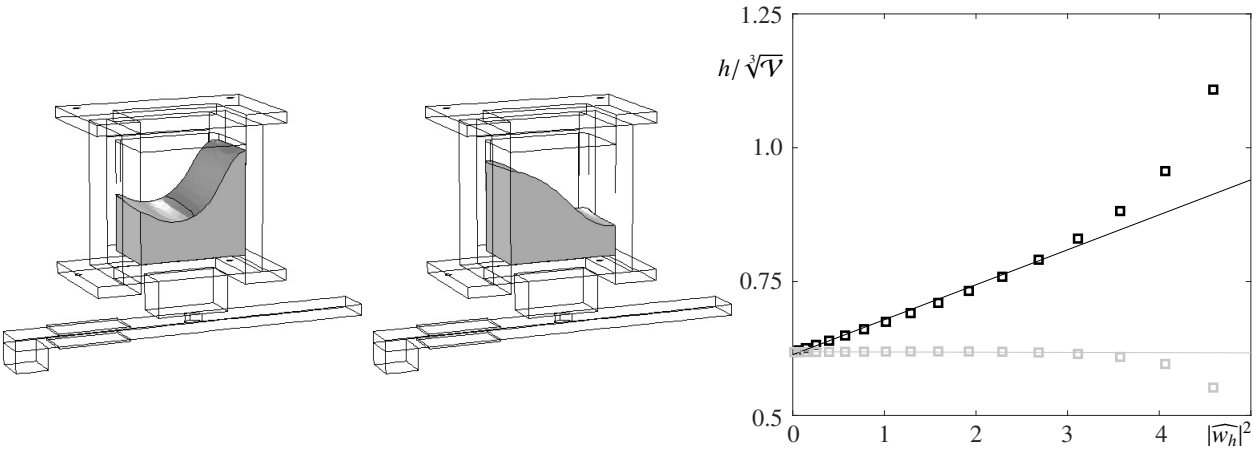


(a) Vibroequilibria, 1st resonant mode (b) Vibroequilibria, 2nd resonant mode (c) Vibroequilibria, 1st resonant mode — $h$ vs. $|\widehat{w_h}|^2$

Figure 5: (a,b) Vibroequilibria calculated numerically for the (a) first and (b) second resonances after 20 s of applied vibrations at 200 V. The parameters used are those of water, with the contact angle set to $\beta = 80°$. (c) Nondimensional height of the front (grey squares) and rear (black squares) contact points at the midplane for increasing vertical vibrational velocity $\widehat{w_h}$ in the first resonance mode. Note the approximately linear dependence on the squared velocity for $|\widehat{w_h}|^2 \lesssim 3$.

cantilever beam and a small rotation around the PMMA piece. Again, the relative displacements are shown in the corresponding inset in Fig. 4.

At a frequency near 1940 Hz, there is a structural mode with less practical interest since very little motion is transmitted to the interior of the fluid. For still higher frequencies, the attenuation increases and the numerical model is less likely to provide an accurate picture of the real response. These high frequency resonances involve a combination of higher beam modes and different structural modes of the container, including both lateral wall motion resembling the breathing of a membrane and similar movement of the aluminium covering plates.

Vibroequilibria states found at the first and second resonances are illustrated in Fig. 5(a,b), respectively, assuming a contact angle of 80°. As described above, the vibroequilibria state depends on the motion of the container and the spatial dependence of the harmonic velocity field that it induces. For the first mode, the fluid tends to climb the right lateral wall due to the more vigorous motion of this boundary, thereby (locally) orienting the surface more perpendicular to the effective oblique vibrational axis. A relatively high voltage of about 100 V or more is needed to observe a significant vibroequilibria effect. The second (counterphase) mode, on the other hand, selects a vibroequilibria state that tends to climb the left wall, which, in this case, vibrates more than the right wall. Again, this can be thought of as a mixture of vertical and horizontal excitations, modified by other types of motion.

Numerical simulations suggest that different modes of the beam, container and fluid can be used to excite various velocity distributions in the fluid. By vibrating the system near one of the resonances, different vibroequilibria solutions can be selected, depending on the type and relative importance of beam and container motion. If up-and-down motion is dominant, for instance, the surface will tend to flatten. In contrast, if the lateral vibration is stronger, a reorientation that tends to locally align the surface with the lateral walls is expected. Between these limiting cases, a range of more complicated mixed solutions can be found. If the dominant vibrations of the system can be predicted, the vibroequilibria effect can be anticipated as well, meaning that the choice of frequency (resonance) in this system is the key factor that selects the shape of the final fluid surface. To this extent, deliberate movement, or control, of the fluid is possible.

Numerical investigations of vibroequilibria solutions were conducted by Fernández at al. (2017)[21] and Gavrilyuk et al. (2004).[24] A general feature of the vibroequilibria effect is its scaling with the square of vibrational (harmonic) velocity or, equivalently, with the dimensionless parameter

$$\xi = |\widehat{\mathbf{u}}_h|^2/4. \tag{16}$$

In Fig. 5(c), we measure the vibroequilibria effect via the height of the rear and front contact points in the midplane and the difference is nearly linear in $|\widehat{w}_h|^2$, until a value of about 3. As discussed in Sec 4, the simplified scheme we use ignores the effect of the free surface deviation on the fast timescale by keeping the same source term in the mean flow equations. Beyond $|\widehat{w}_h| \sim 2$, which corresponds to $V_{pp} = 150$ V, the displacement of the surface is significant (comparable to the fluid depth) so this assumption begins to fail. The figure suggests that the effect of this

DOI: 10.13009/EUCASS2019-224



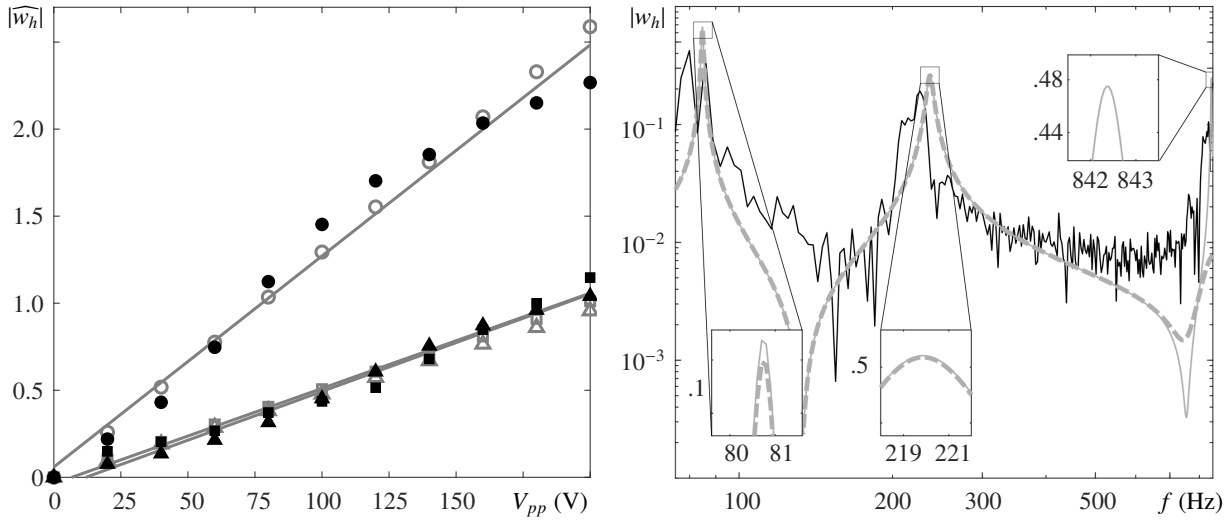


(a) Damping estimation - Velocity fitting

(b) Frequency sweep

Figure 6: (a) Measured magnitude of the vertical harmonic velocity $|\widehat{w_h}|$ at the midpoint of the right endwall for different excitation voltages $V_{pp}$, at the three first natural frequencies: 81 Hz (solid circles), 220 Hz (solid squares) and 842 Hz (solid triangles); with associated linear fittings (grey lines). Values calculated numerically using $\eta_s(f)$ as in Eq. (20) are shown with grey open markers. (b) Magnitude of the vertical harmonic velocity $|w_h|$ for frequencies up to 1 kHz with a driving voltage of 200 V: experimental measurements (black curve) and numerical calculations (grey curves). Two damping models are used: $\eta_s(f)$ [grey solid line, Eq. (20)] and with Rayleigh coefficients [grey dashed line, Eq. (22)]. Close-up views of the three resonances are provided in the insets.

error is to overestimate the vibroequilibria effect, and that an update of the harmonic velocity field is required to go further in amplitude.

## 6. Comparison with experiments

### 6.1 Ground experiments: Damping estimate

In Sec. 5, two different damping values were used to calculate fluid velocities, illustrating the need for a good estimate of the attenuation. An appropriate damping can be determined from tests performed near each resonance by looking at peak amplitude and bandwidth. Both Rayleigh damping $[C]$ and the isotropic loss factor $\eta_s$ are considered by introducing the modified matrices

$$[C] = \alpha_M[\mathcal{M}] + \beta_K[\mathcal{K}], \tag{17a}$$

$$([\mathcal{M}], [\mathcal{K}]) \rightarrow (1 + \mathrm{j}\eta_s)\,([\mathcal{M}], [\mathcal{K}])\,, \tag{17b}$$

in the Finite Element Method formulation. Here, $C$ is the damping matrix, $\mathcal{M}$ and $\mathcal{K}$ are the effective mass and rigidity of the system, respectively, while $\alpha_M$ and $\beta_K$ are the Rayleigh damping coefficients and $\eta_s$ represents the isotropic loss factor.

Experiments indicate that the first three resonances, all at frequencies less than 1 kHz, are of greatest interest since a clear vibroequilibria effect is observed. This means that estimates of the damping coefficients $\eta_s$ (or $\alpha_M$, $\beta_K$) are needed only over frequencies up to 1 kHz, where attention is focused hereafter. Resonances at higher frequencies appear to experience greater damping, which reduces the vibroequilibria effect (i.e., comparable deformation require higher forcing).

As shown in Fig. 6(a), the dependence of measured velocity on applied voltage is nearly linear for the first three modes, with respective linear fits

$$|\widehat{w}_h^{(1)}| = (1.21V_{pp} + 5.91) \cdot 10^{-2}, \tag{18a}$$

$$|\widehat{w}_h^{(2)}| = (0.54V_{pp} - 3.67) \cdot 10^{-2}, \tag{18b}$$

$$|\widehat{w}_h^{(3)}| = (0.56V_{pp} - 6.68) \cdot 10^{-2}, \tag{18c}$$

DOI: 10.13009/EUCASS2019-224



Here, $\widehat{w}_h^{(i)}$ refers to the vertical velocity measured for the $i$th resonant mode, measured at the midpoint of the rear wall of the assembly where the accelerometer is placed.

Neglecting the constant term at $V_{pp} = 0$, which is only finite because of experimental error and filtering effects, the slope of each expression gives the (dimensional) transfer function $|w_h|/V_{pp}$. Based on these values, damping expressions that capture each resonance are determined as functions of frequency. Furthermore, the results of a frequency sweep experiment are shown in Fig. 6(b) (black line) where the bandwidth of each resonance can be estimated.

#### 6.1.1 Isotropic loss factor: $\eta_s(f)$

The damping coefficient $\eta_s$ is chosen to match the predicted velocities at each resonance with those measured from experiments. We use a least squares fitting to determine the coefficients $\mathcal{P}_i$ of a polynomial in frequency

$$\eta_s(f) = \sum_{i=0}^{N} \mathcal{P}_i f^i, \tag{19}$$

and find that a second order fitting polynomial ($N = 2$),

$$\eta_s(f) = -2.573 \cdot 10^{-7} f^2 + 2.337 \cdot 10^{-4} f - 1.093 \cdot 10^{-2}, \tag{20}$$

is sufficient to accurately reproduce the measured results over the frequency range of interest. The vertical velocity distribution obtained after introducing $\eta_s(f)$ into the FEM model is shown in Fig. 6(b) (grey solid curve). The agreement is good, both for the resonance locations and for the maximum velocities.

Despite the success of this approximation over the frequency range of interest, the expression for $\eta_s(f)$ has a negative quadratic coefficient, which gives negative (non-physical) values of the damping at higher frequencies. Extending the model would require a higher order polynomial and is not attempted here because the higher frequency resonance modes involve the cuboid container and cannot be measured well with a single accelerometer.

#### 6.1.2 Rayleigh damping coefficients: $\alpha_M$, $\beta_K$

In an analogous fashion, the Rayleigh damping coefficients can be estimated as a function of the frequency by fitting the resulting values at each resonance. Writing

$$\eta_s = \left( \frac{\alpha_M}{2\pi f} + 2\pi \beta_K f \right), \tag{21}$$

and using the frequencies of the first two resonances, one finds both coefficients:

$$\alpha_M = -2.2594 \ \mathrm{s}^{-1}, \qquad \beta_K = 2.1165 \cdot 10^{-5} \ \mathrm{s}. \tag{22}$$

After introducing $\alpha_M$ and $\beta_K$ into the FEM model, the vertical velocity distribution is calculated and shown in Fig. 6(b) (grey dashed curve). As expected, the velocity at the first two resonances is reproduced quite well, while neither the location nor maximum velocity is captured very accurately for the third resonance. As with the isotropic loss factor, this model does not agree with experimental measurements if the frequency range is extended; a generalization with more frequency-dependent terms would be needed, writing, for example, $\alpha_M(f)$ and $\beta_K(f)$.

### 6.2 Microgravity experiments: Vibroequilibria in the CFVib experiment

The predicted vibroequilibria at the first two resonance modes were illustrated in Fig. 5(a, b) of Sec. 5 for an arbitrary choice of $\eta_s$. Damping does not qualitatively affect the character of these resonance modes, but does affect their width and limit the maximum displacement (equivalently, velocity or acceleration). The attenuation thus affects the voltage required to generate a certain vibroequilibria amplitude (deformation), but has little influence on the shape of the free surface.

Here, we qualitatively compare the numerical predictions with experimental results obtained during the 65th ESA Parabolic Flight Campaign. Some discrepancy is expected owing to flight disturbances and $g$-jitter. Among other sources of error, the midplane symmetry assumed in the model for simplicity and feasibility does not hold in the real experiments.

Reasonable agreement is found between experiment and simulations for the first resonance. Images taken during the microgravity portion of a parabola reveal the tendency of the fluid to climb the rear wall, as seen in Fig 7(a); this behaviour was predicted in Fig. 5(a). Experiments also display surface waves and, sometimes, drop ejection when the

DOI: 10.13009/EUCASS2019-224



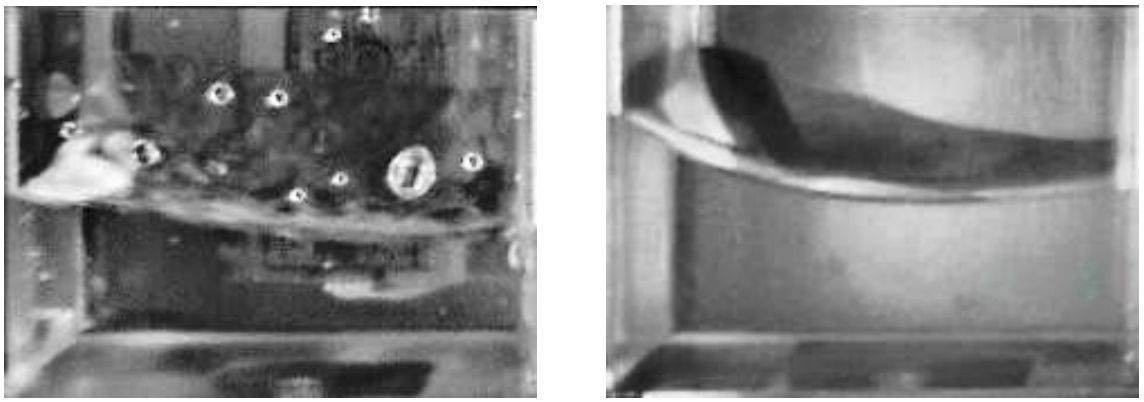

(a) *Vibrated* experiment — Vibroequilibria, 1st resonant mode

(b) *Reference* experiment

Figure 7: Simultaneous images of *Vibrated* and unforced *Reference* microgravity experiments in cuboidal containers partially filled with water: (a) vibroequilibria effect when vibrated at $f \approx 81$ Hz (the first resonant mode) and $V_{pp} = 200$ V, (b) reference experiment, experiencing only the effect of airplane disturbances.

waves are of large amplitude.[18,33] The effects of residual gravity can be seen by comparing the vibroequilibria with the unforced equilibria present in the corresponding passive cell shown in Fig. 7(b). This preliminary analysis makes it clear that flight disturbances are relevant for the results of the experiment, particularly for low to medium applied voltages (up to approximately 100 V) where they can partially mask the vibroequilibria effect.

## 7. CONCLUSIONS

We have described the mathematical and numerical formulation used to model the Control of Fluids with Vibrations (CFVib) microgravity experiment, which flew on the 65th ESA Parabolic Flight campaign. Predictions of the model were compared to experiments on ground and in microgravity.

When a fluid is periodically forced, there are interfacial instabilities like surface waves that occur on this same (fast) timescale and, also, slower (average) processes like the vibroequilibria effect, which describes the reorientation of the fluid interface toward a new quasiequilibrium. In the limit of high amplitude (less in reduced gravity), a free surface or other density contour will tend to position itself (largely) perpendicular to the effective vibrational axis. The physical reason for this is the inhomogeneous dynamic pressure generated by the rapid oscillatory velocity field. This pressure distribution deforms the surface until an appropriate balance with surface tension (and gravity, if present) is achieved.

The CFVib microgravity experiment was designed to study the vibroequilibria effect in small volumes of fluid (dimensions of several centimetres) confined in closed, partially-filled acrylic containers, using vibrations applied via piezoelectric actuators, to deliberately modify the position of the fluid. Cuboidal and cylindrical containers were used with water, silicone oils of different viscosity, and a combination of silicone and vacuum oils. The effect of vibrations was examined under the microgravity conditions of a parabolic flight, in these two geometries and with the selected fluid combinations, and compared to the behaviour of unforced reference cells.

The numerical model developed here was used to understand and complement the experimental results. The piezoelectric ceramics, which are used to deliver vibrations, as well as the structure of the experiment container are treated using classical mechanics theory, while the fluid dynamics is analysed using a separation of timescales. The governing Navier-Stokes equations are expanded in a perturbation series to obtain equations acting on the fast timescale, which provides a linear harmonic velocity field, and on the slow timescale. Compressibility is neglected since the container size is much smaller than the wavelength of sound over the frequency range of interest (up to 1 kHz). The separation between the period of the harmonic field oscillating at frequency $\omega$ and the longer time needed for relaxing to either a static equilibrium or a vibroequilibria state justifies the neglect of transient behaviour for the harmonic field and its resolution in the frequency domain. The linear problem on the fast timescale includes the fluid-structure interaction along the container walls and provides the (nonlinear) source term for the equations on the slow timescale. The numerical scheme can be further simplified if the surface deformation is assumed small enough that it does not significantly affect the harmonic velocity field, an approximation that fails at high enough forcing. Whether the harmonic velocity field is updated or not, the evolution towards the vibroequilibria is completed after the surface reaches a steady (on the slow timescale) position. As anticipated, the time for this relaxation is on the order of a few seconds, several orders of magnitude larger than the period of piezoelectric vibrations.

DOI: 10.13009/EUCASS2019-224



Experiments and simulations are consistent and suggest that one can take advantage of the different resonant modes of the experimental assembly to excite distinct oscillatory velocity fields in the fluid, and thereby achieve different vibroequilibria solutions. If, for example, the dominant motion of the container is up-and-down, the surface will tend to flatten "horizontally". If the dominant vibration is along a lateral axis, the fluid will tend to climb the lateral walls of the container (into a more "vertical" orientation). A wide variety of intermediate scenarios can occur, generating vibroequilibria of a more complicated (mixed) type. The results presented here thereby offer support for the idea that vibrations can be used to deliberately reorient fluid interfaces, while the numerical model allows us to predict the vibroequilibria effect associated with the main resonant modes of the system. A more detailed analysis of the experimental results should allow the model to be further refined and improved.

## Acknowledgments

This work was supported by the ESA Education Office in connection with the Fly Your Thesis! programme and the 65th ESA Parabolic Flight Campaign, and by the Ministerio de Economía y Competitividad under Projects No. ESP2013-45432-P and No. ESP2015-70458-P. We thank the European Low Gravity Research Association (ELGRA) for their valuable scientific support and Novespace for their technical advice and contributions during the project. We thank Trenz Electronic for their Analog Discovery device, Analog Devices (ADI) for providing the accelerometers, and Krytox™ Performance Lubricants, a business of The Chemours Company, for supplying the vacuum oil. Finally, we thank the Spanish User Support and Operations Centre (E-USOC) and the Escuela Técnica Superior de Ingeniería Aeronáutica y del Espacio at the Universidad Politécnica de Madrid, which have supported this project from the beginning.

## References

[1] M. Faraday. On peculiar class of acoustical figures; and on certain forms assumed by groups of particles upon vibrating elastic surfaces. *Philos. Trans. R. Soc. Lond.*, 121:299–340, 1831.

[2] G. H. Wolf. Dynamic stabilization of the interchange instability of a liquid-gas interface. *Phys. Rev. Lett.*, 24(9):444–446, 1970.

[3] J. W. Miles. Resonantly forced surface waves in a circular cylinder. *J. Fluid Mech.*, 149:15–31, 1984.

[4] J. W. Miles and D. M. Henderson. Parametrically forced surface-waves. *Annu. Rev. Fluid Mech.*, 22:143–165, 1990.

[5] H. Arbell and J. Fineberg. Pattern formation in two-frequency forced parametric waves. *Phys. Rev. E*, 65:036224, 2002.

[6] T. B. Benjamin and F. Ursell. The stability of the plane free surface of a liquid in vertical periodic motion. *Proc. R. Soc. Lond. A Math. Phys. Sci.*, 225(1163):505–515, 1954.

[7] K. Kumar and L. S. Tuckerman. Parametric instability of the interface between two fluids. *J. Fluid Mech.*, 279:49–68, 1994.

[8] C. J. R. Garrett. On cross-waves. *J. Fluid Mech.*, 41:837–849, 1970.

[9] J. Porter, I. Tinao, A. Laveron-Simavilla, and C. A. Lopez. Pattern selection in a horizontally vibrated container. *Fluid Dyn. Res.*, 44(6):65501, 2012.

[10] F. Varas and J. M. Vega. Modulated surface waves in large-aspect-ratio horizontally vibrated containers. *J. Fluid Mech.*, 94:022216, 2016.

[11] P. Salgado Sanchez, J. Porter, I. Tinao, and A. Laveron-Simavilla. Dynamics of weakly coupled parametrically forced oscillators. *Phys. Rev. E*, 579:271–304, 2007.

[12] D. V. Lyubimov and A. A. Cherepanov. Development of a steady relief at the interface of fluids in a vibrational field. *Fluid Dyn.*, 21(6):849–854, 1986.

[13] E. Talib, S. V. Jalikop, and A. Juel. The influence of viscosity on the frozen wave stability: theory and experiment. *J. Fluid Mech.*, 584:45–68, 2007.

DOI: 10.13009/EUCASS2019-224



[14] T. P. Lyubimova, A. O. Ivantsov, Y. Garrabos, C. Lecoutre, G. Gandikota, and D. Beysens. Band instability in near-critical fluids subjected to vibration under weightlessness. *Phys. Rev. E*, 95:013105, 2017.

[15] D. Beysens, Y. Garrabos, D. Chatain, and P. Evesque. Phase transition under forced vibrations in critical CO2. *EPL*, 86, 2009.

[16] Y. A. Gaponenko, M. M. Torregrosa, V. Yasnou, A. Mialdun, and V. Shevtsova. Dynamics of the interface between miscible liquids subjected to horizontal vibration. *J. Fluid Mech.*, 784:342–372, 2016.

[17] V. Shevtsova, Y. A. Gaponenko, V. Yasnou, A. Mialdun, and A. Nepomnyashchy. Two-scale wave patterns on a periodically excited miscible liquid-liquid interface. *J. Fluid Mech.*, 795:409–422, 2016.

[18] P. Salgado Sanchez, V. Yasnou, Y. A. Gaponenko, A. Mialdun, J. Porter, and V. Shevtsova. Interfacial phenomena in immiscible liquids subjected to vibrations in microgravity. *J. Fluid Mech.*, 865:850–884, 2019.

[19] G. Gandikota, D. Chatain, S. Amiroudine, T. Lyubimova, and D. Beysens. Frozen-wave instability in near-critical hydrogen subjected to horizontal vibration under various gravity fields. *Phys. Rev. E*, 89:012309, 2014.

[20] P. Salgado Sanchez, Y. A. Gaponenko, J. Porter, and V. Shevtsova. Finite-size effects on pattern selection in immiscible fluids subjected to horizontal vibrations in weightlessness. *Phys. Rev. E*, 99(4):042803, 2019.

[21] J. Fernandez, I. Tinao, J. Porter, and A. Laveron-Simavilla. Instabilities of vibroequilibria in rectangular containers. *Phys. Fluids*, 29(2):24108, 2017.

[22] D. Beysens. Vibrations in space as an artificial gravity? *Europhysics News*, 37(3):22–25, 2006.

[23] J. Fernandez, P. Salgado Sanchez, I. Tinao, J. Porter, and J. M. Ezquerro. The CFVib experiment: Control of Fluids in Microgravity with Vibrations. *Microgravity Sci. Technol.*, 29(5):351–364, 2017.

[24] I. Gavrilyuk, I. Lukovsky, and A. Timokha. Two-dimensional variational vibroequilibria and Faraday's drops. *J. Appl. Math. Mech.*, 55(6):1015–1033, 2004.

[25] L. D. Landau and E. M. Lifshitz. *Fluid Mechanics*. Pergamon books Ltd., 1987.

[26] V. Pletser, S. Rouquette, U. Friedrich, J. F. Clervoy, T. Gharib, F. Gai, and C. Mora. The first european parabolic flight campaign with the airbus A310 ZERO-G. *Microgravity Sci. Technol.*, 28(6):587–301, 2016.

[27] M. Richard. Piezoelectricity. *Phys. Rev. B*, 5(4):1607–1613, 1972.

[28] S. O. Catarino, J. M. Miranda, S. Lanceros-Mendez, and G. Minas. Modeling and simulation of acoustic streaming phenomenon produced by piezoelectric polymers. *Proc. ENGBENG*, 5, 2011.

[29] S. Sherrit and B. K. Mukherjee. Characterization of piezoelectric materials for transdurcers. Technical report, 2007.

[30] https://www.comsol.com/.

[31] D. Koster. *Numerical Simulation of Acoustic Streaming on SAW-driven Biochips*. 2006.

[32] H. N. Abramson. The dynamic behavior of liquids in moving containers, with applications to space vehicle technology. Technical report, NASA, 1966.

[33] A. J. James, M. K. Smith, and A. Glezer. Vibration-induced drop atomization and the numerical simulation of low-frequency single-droplet ejection. *J. Fluid Mech.*, 476:29–62, 2003.